DES 2019-0048
Fermilab PUB-19-114-AE

MNRAS **000**, 1–18 (2019) Preprint April 10, 2019 Compiled using MNRAS LaTeX style file v3.0

arXiv:1904.04350v1 [astro-ph.GA] 8 Apr 2019

Modelling the Milky Way. I - Method and first results fitting the thick disk and halo with DES-Y3 data

A. Pieres*[1,2], L. Girardi[1,3], E. Balbinot[4], B. Santiago[1,5], L. N. da Costa[1,2], A. Carnero Rosell[1,6], A. B. Pace[7], K. Bechtol[8], M. A. T. Groenewegen[9], A. Drlica-Wagner[10,11], T. S. Li[10,11], M. A. G. Maia[1,2], R. L. C. Ogando[1,2], M. dal Ponte[1,5], H. T. Diehl[10], A. Amara[12], S. Avila[13], E. Bertin[14,15], D. Brooks[16], D. L. Burke[17,18], M. Carrasco Kind[19,20], J. Carretero[21], J. De Vicente[6], S. Desai[22], T. F. Eifler[23,24], B. Flaugher[10], P. Fosalba[25,26], J. Frieman[10,11], J. García-Bellido[13], E. Gaztanaga[25,26], D. W. Gerdes[27,28], D. Gruen[17,18,29], R. A. Gruendl[19,20], J. Gschwend[1,2], G. Gutierrez[10], D. L. Hollowood[30], K. Honscheid[31,32], D. J. James[33], K. Kuehn[34], N. Kuropatkin[10], J. L. Marshall[7], R. Miquel[21,35], A. A. Plazas[36], E. Sanchez[6], S. Serrano[25,26], I. Sevilla-Noarbe[6], E. Sheldon[37], M. Smith[38], M. Soares-Santos[39], F. Sobreira[1,40], E. Suchyta[41], M. E. C. Swanson[20], G. Tarle[28], D. Thomas[42], V. Vikram[43], A. R. Walker[44]
Affiliations are listed after the references

Accepted in XX YY 2019. Received 08 April 2019

ABSTRACT

We present MWFITTING, a method to fit the stellar components of the Galaxy by comparing Hess Diagrams (HDs) from TRILEGAL models to real data. We apply MWFITTING to photometric data from the first three years of the Dark Energy Survey (DES). After removing regions containing known resolved stellar systems such as globular clusters, dwarf galaxies, nearby galaxies, the Large Magellanic Cloud and the Sagittarius Stream, our main sample spans a total area of ∼2,300 deg^2 distributed across the DES footprint. We further explore a smaller subset (∼ 1,300 deg^2) that excludes all regions with known stellar streams and stellar overdensities. Validation tests on synthetic data possessing similar properties to the DES data show that the method is able to recover input parameters with a precision better than 3%. Based on the best-fit models, we create simulated stellar catalogues covering the whole DES footprint down to $g = 24$ magnitude. Comparisons of data and simulations provide evidence for a break in the power law index describing the stellar density of the Milky Way (MW) halo. Several previously discovered stellar over-densities are recovered in the residual stellar density map, showing the reliability of MWFITTING in determining the Galactic components. Simulations made with the best-fitting parameters are a promising way to predict MW star counts for surveys such as LSST and Euclid.

Key words: Milky Way, structure; stellar models

1 INTRODUCTION

Over the last 40 years, we have learned (Bahcall & Soneira 1981) the usefulness of describing a complex system like the Milky Way (MW) through simple building blocks, composed of nearly homogeneous stellar populations, smoothly

---

* E-mail: adriano.pieres@linea.gov.br

distributed in space in a few components like the thin and thick disks, bulge and halo. The derivation of simple parameters for these components – such as scale lengths and heights, limiting radii, central densities, etc. – allows us to put our Galaxy in perspective, comparing it to other spiral galaxies (Courteau et al. 2011), and to galaxies produced in cosmological simulations (see, e.g. Hopkins et al. 2014; Bland-Hawthorn & Gerhard 2016). Examining the residuals of the best-fit models enables the identification of stellar substructure such as dwarf galaxies and stellar streams (e.g., Shipp et al. 2018). Fitted models can also be used to estimate the distribution of stars in future surveys.

Our understanding of the MW has steadily advanced over the past several decades. For example, the thick disk (Gilmore & Reid 1983) has long been proposed to explain the MW stellar population within 1-5 kpc on either side of the Galactic plane. Thick disk stars differ from those closer to the Galactic plane in kinematics, age and metallicity, being older, more metal-poor, less rotationally supported, and having typically higher [α/Fe] at a fixed metalicity (for instance, see Reddy et al. 2006; Fuhrmann 2008). More recently, the spatial structure of different stellar populations has been studied by Anders et al. (2014) and Bovy et al. (2016), among others, using survey data, specifically from APOGEE (Majewski et al. 2016). In brief, high [α/Fe] stars tend to follow a double exponential density profile parallel and perpendicular to the Galactic plane, with scales of $h_R \simeq 2.2$ kpc and $h_z \simeq 1.0$ kpc, respectively (Bovy et al. 2016). The lower [α/Fe] stars display a more complex distribution, including a metalicity gradient and disk flaring (Anders et al. 2014). Even so, the traditional description of the thin and thick disk components with double exponential profiles (or a $\mathrm{sech}^2 z$ perpendicular to the disk plane) is adequate (Cabrera-Lavers et al. 2005; Jurić et al. 2008; de Jong et al. 2010). Even with a reasonably good empirical description for the distribution of stars in both disks, their formation is still a puzzle for the astronomical community (Chiba & Beers 2000; Bensby et al. 2003; Brook et al. 2004; Villalobos & Helmi 2008; Bournaud et al. 2009; Schönrich & Binney 2009; Bensby & Feltzing 2010; Loebman et al. 2011; Steinmetz 2012; Minchev et al. 2015; Helmi et al. 2018).

In the outer limits of the MW, the stellar Galactic halo extends in a roughly spherical shape, and recent works (Jurić et al. 2008; de Jong et al. 2010) indicate that a power law better describes the stars in that component than an exponential profile. Work focusing on the halo have found evidence for a break in the stellar density profile at ∼30 kpc (Watkins et al. 2009; Deason et al. 2011; Sesar et al. 2011) or further (Deason et al. 2018), at distances where discrete stellar overdensities and streams are visible. In this way, other works focusing on the outer regions of the halo show that the power law exponent is steeper than that of the inner regions (see, e.g. Slater et al. 2016).

In addition to the aforementioned developments in describing the stellar content of the Galaxy, an impressive amount of work has been dedicated to gauge the star formation rate (SFR, Ryan & Norris 1991; Fuhrmann 1998), initial mass function (IMF, Kroupa 2001; Chabrier 2003; Kroupa & Weidner 2003), and Age-Metalicity Relation (AMR, Rocha-Pinto et al. 2000; Zoccali et al. 2003; Fuhrmann 2008) for the stars in the MW, along with the modelling of stellar evolution (Bertelli et al. 1994; Girardi et al. 2000, 2002; VandenBerg et al. 2006; Marigo & Girardi 2007; Girardi et al. 2010; Paxton et al. 2011; Spada et al. 2013) and the stellar contents of the Galaxy itself (Sharma et al. 2011; Czekaj et al. 2014[1]; Pasetto et al. 2018). Thanks to all these developments, we are now able to build a detailed structural model for the Galaxy.

To take advantage of this knowledge and the increasing number of deep wide-field astronomical surveys, we have developed MWFITTING method. This work aims to present the method and to show its first application to data in the Dark Energy Survey (DES; DES Collaboration 2005).

In this work we aim to:

- Present an efficient method to describe the structure of the Galaxy by comparing star counts to predictions of stellar population synthesis models. The comparison between data and models is made through colour-magnitude bins (i.e., Hess Diagram, HD) in specific regions in the sky. Many different models are considered to model star counts, such as the spatial distribution of stars in the MW components, the stellar IMF, SFR, and AMR. Also crucial in determining star counts are the input stellar evolutionary models that prescribe magnitudes and colours as a function of fundamental stellar parameters, such as mass, age, and metallicity.
- Validate the code using mock data. These tests are done to test the accuracy of MWFITTING to evaluate systematic uncertainties, and to measure the effect of initial values has on recovering the input parameters.
- Apply MWFITTING to model the Galactic thick disk and halo in DES year 3 (Y3) data.
- Show and discuss the results of the method and the implications on the Galactic model adopted.

This paper is structured as follows: in Section 2 we discuss the MWFITTING method. In Section 3 we briefly describe the DES year 3 data. In Section 4 we present the results of MWFITTING method. In Section 5 we describe a simulation based on the best fitting parameters and discussion of the results. Finally, we conclude in Section 6.

2 MWFITTING METHOD

In this paper, we adopt TRILEGAL[2] models to describe the stellar content of the Galaxy. TRILEGAL is a stellar population synthesis code, based on the Girardi et al. (2002) database of stellar isochrones, and augmented with models for brown and white dwarfs. For more details about the stellar models, we refer to Girardi et al. (2005). Note that even though several upgrades in the database of evolutionary tracks and stellar atmospheres have become available recently (see, e.g. Marigo et al. 2017), they severely reduce computational speed, and only include short-lived evolutionary phases and cool stars, which are not the subject of the present work.

The following subsections present the sequence of steps that leads to a final product of the MWFITTING method. Section 2.1 describes TRILEGAL input parameters to model

---

[1] See `https://model.obs-besancon.fr/modele_ref.php` for a complete list of publications of the Besançon group.

[2] `http://stev.oapd.inaf.it/cgi-bin/trilegal`

a sky region with a specific Galactic model. The previous attempts to calibrate the Galactic model using TRILEGAL are briefly discussed in Section 2.2; the adopted Galactic model is presented in Section 2.3; in Section 2.4 we discuss the implementation of the MWFITTING method and in Section 2.5 we validate the MWFITTING pipeline, using synthetic data with known inputs and recover the simulated parameters.

2.1 Trilegal parameters

The TRILEGAL population synthesis simulation requires input parameters such as: covered area, photometric system, filters, magnitudes and colour ranges, 3D position of the Sun, dust distribution, IMF for single stars, binary fraction, and mass ratios of unresolved binaries.

The pipeline requires structural models, SFR, and AMR for each Galactic component (see Table 1).

Regarding the color and magnitude ranges, the TRILEGAL models are very successful in describing the stellar evolutionary phases as the main sequence (MS), including the turn-off (MSTO), and stars in the sub and red giant branches (respectively, SGB and RGB), for stars in a wide range of masses.

Historically, the stellar evolutionary models present a poor colour-fit for low-mass stars with [Fe/H] $\geqslant$ -2, as the M stars, the most abundant spectral type in thin disk.

See for instance (Sarajedini et al. 2007), for a discussion about the comparisons of simple stellar populations of globular clusters to theoretical models.

Based on that, we choose to exclude the red thin-disk stars (see figure 2 and discussion in de Jong et al. 2010) and keep the parameters of this component fixed. The magnitude depth of DES also favours stars farther away than those in the thin disk, whats supports our choice.

2.2 Previous attempts to calibrate Trilegal

Early descriptions of the MW components and their calibrations using TRILEGAL are found in Groenewegen et al. (2002) and Girardi et al. (2005). Those first attempts were based on a simple trial-and-error approach, where each model parameter was set to literature values, changed by hand until a "good description" for the star counts was met for a given survey. Surveys used in these analyses compromise both deep (e.g., DMS and EIS-deep Osmer et al. 1998; Arnouts et al. 2001), shallow (e.g., 2MASS Skrutskie et al. 2006) photometric data, and local (e.g., *Hipparcos* catalog Perryman et al. 1997).

Vanhollebeke et al. (2009) explored a different approach to calibrate the bulge's parameters using TRILEGAL. They defined a likelihood function to quantitatively evaluate the goodness-of-fit between data and model (see also Eidelman et al. 2004; Dolphin 2002) as:

$$-2\ln\lambda(\theta) = 2\sum_{i=1}^{N}\left(\nu_i(\theta) - n_i + n_i \ln\frac{n_i}{\nu_i(\theta)}\right) \quad (1)$$

where n_i is the number of observed objects in a given magnitude/colour bin i, and $\nu_i(\theta)$ is the number of objects predicted by the set of parameters θ that describes the model. The summation is performed over all lines-of-sight, and magnitude/colour bins included in the comparison. The authors used the Broyden-Fletcher-Goldfarb-Shanno (BFGS) algorithm (Fletcher 1987) to maximize their likelihood and derived uncertainties from the likelihood profile, as detailed out in that work.

In this context, the fitting of disk and halo parameters using the latter method requires an extra set of variables. This presents several issues:

- Fitting the disk (thin and thick) and halo implies the simultaneous fitting of ~ 30 structural parameters, with many samples across the sky. The resulting analysis is very time-consuming.
- Local maxima in likelihood space may be very common, and due to the high dimensionality of the problem finding absolute maxima may be challenging.

This is not the case when fitting the bulge, as there are less parameters, and there are a large set of lines-of-sight which leaves little chance for solutions to be trapped in local maxima (Vanhollebeke et al. 2009). In the present case, it is advisable to implement tests for local maxima in log-likelihood space, and check whether different starting conditions lead to the same solution. These tests imply even longer computing times.

In the next sections, we describe the implementation of an algorithm that tackles the challenges discussed above (see also Girardi et al. 2012).

2.3 Galactic model adopted

Table 1 summarizes the functional form utilized for each Galactic component, the parameters that describe the component, and whether the parameter is fixed or free in the fit of the present paper. We adopt an exponential model along the disk plane and a square hyperbolic secant perpendicular to it for the thin disk. The only parameters allowed to vary are related to the thick disk and to the halo of our Galaxy. The parameters of the thin disk and bulge modelled by TRILEGAL in this work are kept fixed at the values described in Girardi et al. (2005), with some minor tweaks as in Girardi et al. (2012). An exponential model in both radial and vertical directions describes the distribution of stars in the thick disk. The stellar halo is described by a power law model (Jurić et al. 2008; de Jong et al. 2010).

Considering the Galactic center, DES covers the South Galactic cap down to $b = -30^{\circ}$, virtually excluding the MW bulge. We fix the parameters of the bulge component, following the triaxial model presented in Binney et al. (1997).

The IMF assumed for Galactic stars is the Chabrier lognormal IMF (Chabrier 2003) and the occurrence of binaries are adopted as 30%, being the mass ratio of the secondary over the primary limited between 0.7 and 1.0. The SFR and AMR are specific to each MW component. Simulated stars in the bulge and in the thick disk follow a SFR and AMR described by Zoccali et al. (2003) and Boeche et al. (2013), respectively. Thin disk and halo stars are modelled following previous comparisons from Groenewegen et al. (2002) and Girardi et al. (2005).

Table 1. The MW model, its components and parameters adopted in this work. The columns list: the formula for each MW component (first), free parameters (second), meaning (third one), units (forth column), initial value (fifth column) and the best-fit value with errors (last column) for both samples († for *raw* sample and ‡ for *refined* sample). The MW model includes the bulge as a triaxial truncated spheroid component, the thin disk described by an exponential model in radial axis and a square secant model in the vertical axis, an exponential thick disk in both directions and a halo detailed by a power law.

Formula	Symbol	Meaning	Unit	Initial value	Fixed/Best-fit value⋆
Bulge[1]					
$\rho^{\rm bulge} = \rho_{GC}^{\rm bulge}\dfrac{\exp(-a^2/a_m^2)}{(1+a/a_0)^{1.8}}$	$\rho_{\rm GC}^{\rm bulge}$	space density at GC	$\rm M_\odot\,pc^{-3}$	400	fixed
with $\rho^{\rm bulge}(0,0,0) = \rho_{\rm GC}^{\rm bulge}$	$a_{\rm m}$	scale length	pc	2500	fixed
with $a = \left(x'^2 + y'^2/\eta^2 + z^2/\zeta^2\right)^{1/2}$	a_0	truncation scale length	pc	95	fixed
and x', y' rotated by ϕ_0. w.r.t. x, y	η, ζ	1:η:ζ scale ratios	-	0.68, 0.31	fixed
	ϕ_0	angle w.r.t. Sun–GC line	deg (°)	15	fixed
Thin disk					
$\rho^{\rm thin} = A^{\rm thin}{\rm sech}^2(h/h_z^{\rm thin}) \times$	$\Sigma_\odot^{\rm thin}$	local mass surface density	$\rm M_\odot\,pc^{-2}$	55.41[2]	fixed
$\exp(R/h_R^{\rm thin})$	$h_R^{\rm thin}$	thin disk scale length	pc	2913[2]	fixed
with $h_z^{\rm thin} = h_{z,0}^{\rm thin} + \left(1 + t/t_{\rm incr}^{\rm thin}\right)^\alpha$	$R_{\rm max}^{\rm thin}$	maximum radius	kpc	15	fixed
and $\displaystyle\int_{h=-\infty}^{+\infty} \rho^{\rm thin}{\rm d}z\Big\vert_\odot = \Sigma_\odot^{\rm thin}$	$h_{z,0}^{\rm thin}$	scale height for youngest stars	pc	94.7[2]	fixed
	$t_{\rm incr}^{\rm thin}$	timescale for increase in h_z	Gyr	5.55[2]	fixed
	α	exponent for increase in h_z	-	1.67[3]	fixed
Thick disk					
$\rho^{\rm thick} = A^{\rm thick}\exp(h/h_z^{thick}) \times$	$h_z^{\rm thick}$	scale height	pc	819.0	$819.0 \pm 7.0^\dagger$ $824.0 \pm 7.0^\ddagger$
$\exp(R/h_R^{\rm thick})$	$h_R^{\rm thick}$	thick disk scale length	pc	2293	$2293 \pm 32^\dagger$ $2284 \pm 166^\ddagger$
with $\displaystyle\int_{h=-\infty}^{+\infty} \rho^{\rm thick}{\rm d}z\Big\vert_\odot = \Sigma_\odot^{\rm thick}$	$\Sigma_\odot^{\rm thick}$	local mass surface density	$10^{-3}\rm M_\odot\,pc^{-2}$	4.16	$4.16 \pm 0.10^\dagger$ $4.02 \pm 0.15^\ddagger$
	$R_{\rm max}^{\rm thick}$	maximum radius (fixed)	kpc	15	fixed
Halo					
$\rho^{\rm halo} = \rho_\odot^{\rm halo}\left(\dfrac{r_\odot}{\sqrt{R^2 + (z/q)^2}}\right)^n$	n	exponent	-	2.590	$2.590 \pm 0.025^\dagger$ $2.625 \pm 0.026^\ddagger$
with $\rho^{\rm halo}(R_\odot, 0, z_\odot) = \rho_\odot^{\rm halo}$	q	axial ratio z/x (oblateness)	-	0.637	$0.637 \pm 0.009^\dagger$ $0.618 \pm 0.014^\ddagger$
	$\rho_\odot^{\rm halo}$	local mass space density	$10^{-5}\rm M_\odot\,pc^{-3}$	5.25	$5.25 \pm 0.10^\dagger$ $5.54 \pm 0.12^\ddagger$
Dust layer					
$\rho^{\rm dust} = A^{\rm dust}\exp(h/h_z^{\rm dust})$	A_V^∞	total extinction at infinity	-	[4]	fixed
with $\displaystyle\int_{\ell=0}^{+\infty} \rho^{\rm dust}{\rm d}\ell = A_V^\infty$	$h_z^{\rm dust}$	dust scale height	pc	110[5]	fixed
Others					
	$R_\odot$	Sun's distance to the GC	kpc	8.7[1]	fixed
	$z_\odot$	Sun's height above the plane	pc	24.2[6]	fixed

[1] Parameters from Vanhollebeke et al. (2009)
[2] Best-fit parameter from Girardi et al. (2005)
[3] Adopted in Girardi et al. (2005)
[4] Schlegel et al. (1998)
[5] Lynga (1982)
[6] Maíz-Apellániz (2001)
⋆ See Table 3 for more details about those parameters.

2.4 The MWFitting method: fitting the galaxy with Hess diagrams

The MWFITTING method consists of fitting a global, multi-component model of the MW to the observed stellar density in bins of Galactic longitude and latitude, magnitude, and color. The inclusion of spatial and color-magnitude information allows us to break degeneracies between the various MW model components.

We begin by pixelizing the sky using the HEALPix[3] scheme to define individual lines-of-sight (which we call "cells"). We select cells that reside within the survey, and remove cells that are contaminated by resolved stellar populations such as globular clusters and dwarf galaxies. In this paper we also exclude regions at low Galactic latitude, since we are focusing on fitting the MW halo and thick disk components. For each cell, we calculate the coordinates of the centre, the average reddening and reddening dispersion, the limiting magnitude (as specified by user), the colour range, and the bin size in the color-magnitude diagram (CMD) space.

Within each cell, we calculate model HDs for each component (i.e., bulge, halo, thin, and thick disk) over a range of distances, typically binned in 10 pc. These so-called "partial HDs" for each component and distance are stored in separate Header Data Units (HDUs) of a multi-extension FITS[4] file. This data format allows the normalizations of different model components to be quickly adjusted. For example, the normalization of the stellar halo can be adjusted by a factor f, by multiplying all partial HDs associated with the halo by the same factor f. The total model-predicted MW HD can be quickly calculated from a linear combination of the individual partial HDs. This method allows us to rapidly construct stellar density predictions for a wide range of MW model parameters as listed in Table 1. Variation in each parameter corresponds to varying the weight of each partial HD, which are then combined to produce a total HD in each HEALPix cell.

The Poisson log-likelihood (Eq. 1) is calculated by first comparing the total model-predicted HDs to the data in each cell and then summing the log-likelihoods over all cells. To fit the MW model to an observed data set, we apply an Affine Invariant Markov Chain Monte Carlo (MCMC) Ensemble sampler (Foreman-Mackey et al. 2013, i.e., EMCEE). The free and fixed parameters of our model, along with their initial values, are listed in Table 1. We assume flat priors ranging from 0.5-2.0 times the initial value of each free model parameter. We also checked visually whether the walkers converged or not at the end of the burn-in phase, in order to inform realistic best-fitting parameters.

Since for each cell, TRILEGAL computes as discrete distribution of points as a realization of the expected population of stars in the CMD space to each cell, we are left with statistical noise due to the point process. To mitigate this noise, we increase the number of simulated stars by an *over-factor* which is then taken into account while normalizing the final Hess diagram for each cell. A typical *over-factor* value is 30, for the magnitude, colour range, and MW components explored in this work.

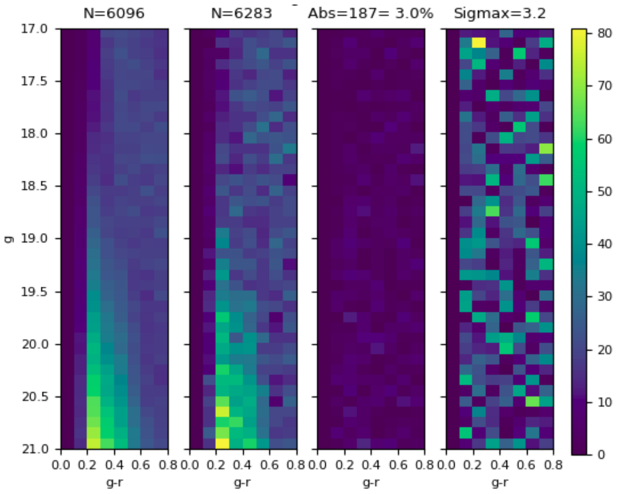

Figure 1. HDs for the cell with the largest difference in star counts between the mock data and the best-fit data in test A. *Leftmost HD:* best-fit model. *Second from the left:* input mock data. *Second from the right:* absolute differences between mock data and the best-fit model. These three HDs are colour-coded by star counts according to the colour bar. *Rightmost panel:* Poissonian significance, normalized by the maximum significance ($\sigma_{max} = 3.2$). In this case, the colour code is different from that of the colour bar. The title indicates the number of stars (first and second panel), absolute difference (third panel), and the maximum of the Poisson significance (fourth panel).

The MWFITTING code was developed and is currently implemented in the DES-Brazil Portal powered by Laboratório Interinstitucional de e-Astronomia (LIneA[5]). More details on the DES-Brazil Portal can be found in Gschwend et al. (2018) and Fausti Neto et al. (2018). The application of MWFITTING to the DES data took 23h in a SGI ICE-X FC3Y cluster with 4 cores. Each node contained 48 cores and 125 GB of RAM.

2.5 Validating the code with mock data

In this section we describe MWFITTING tests applied to mock data. We verify that we can recover the input parameters of our simulated data set when applied to an area with the same footprint as DES-Y3.

Each test utilizes 80 cells, and each cell has the same area as the unit cell designed for the real data (HEALPIX pixels with NSIDE=16), following identical footprint and coverage maps (see Section 3). The range in magnitude and colour is the same as the DES data ($17 < g < 21$ and $0.0 < g - r < 0.8$, respectively), with the same bin in magnitude and color space (0.1). Uncertainties were not incorporated in the synthetic data, since Balbinot et al. (2015) report that magnitude errors for $r \leqslant 21$ are typically $\simeq$0.02 and smaller for brighter stars.

Table 2 lists the parameters, units, input values, best-fit values and their errors, as indicated by EMCEE, and the significance of the differences between the best-fit and the true value, for two processes. We run two tests with the same

---

[3] `https://healpix.jpl.nasa.gov/`

[4] `https:////fits.gsfc.nasa.gov/fits_standard.html`

[5] `http://www.linea.gov.br/`

Table 2. Results of two tests (A and B) using MWFITTING. Even though the initial guesses start far from the input values, the final parameter values are within $\simeq$ 3% of the input values, however, the parameter values are within 3σ when considering the model uncertainites (last two columns). The simulations in this table compare 80 fields and oversample the models in the same way as the comparison to real data.

Parameter	*Unit*	*True Value*	*Initial Guess*		*Best-fitting*		$\frac{\lvert Best-True\rvert}{True}$ (%)		$\frac{Best-True}{\sigma}$	
			A	B	A	B	A	B	A	B
ThickDisk h_e	pc	754.9	1123.4	512.1	$750.7^{+1.8}_{-1.8}$	$748.9^{+1.7}_{-1.9}$	0.6	0.8	-2.3	-3.0
ThickDisk R_e	pc	2163	2722	1613	2156^{+12}_{-6}	2157^{+6}_{-6}	0.3	0.3	-0.7	-1.0
ThickDisk ρ (R=R$_\odot$)	$\times10^{-3}$M$_\odot$pc^{-2}	4.98	6.16	6.76	$5.07^{+0.04}_{-0.04}$	$5.08^{+0.04}_{-0.03}$	1.9	2.1	+2.3	+2.7
Halo n	-	2.398	3.168	2.715	$2.411^{+0.008}_{-0.006}$	$2.415^{+0.006}_{-0.006}$	0.5	0.7	+1.9	+2.8
Halo q	-	0.683	0.820	0.519	$0.687^{+0.005}_{-0.003}$	$0.680^{+0.002}_{-0.002}$	0.6	0.4	+1.0	-1.5
Halo ρ (R=R$_\odot$)	$\times10^{-5}$ M$_\odot$pc^{-3}	4.36	5.96	3.81	$4.41^{+0.03}_{-0.04}$	$4.49^{+0.05}_{-0.04}$	1.1	3.0	+1.4	+2.6

input parameters but different initial values for the MCMC, which we refer to as test A and B.

Analyzing Table 2, we show MWFITTING is able to recover the input values of the mock data accurately, even when the initial starting points are far from the true ones. Differences between true and best-fit values are $\simeq$ 3% of the true parameters at the maximum, and the deviations are within 3σ in all cases. The maximum differences occur for the density, while the differences for the remaining parameters are all below 1%.

Inspecting the HDs diagrams, there is an excellent concordance between the mock data and the best-fit model data. The overall range of differences in the process of test A between input data and best-fit models is [-2.71%, +2.97%], in terms of star counts. Fig. 1 shows the HDs of the cell with the largest difference (+2.97%), located at [l = 218.21°, $b = -71.44$°]. Panels of Fig. 1 shows the HD of the best-fit model, simulated input data (mock), absolute difference, and the Poissonian significance over the HD cells, limited by the maximum significance (given in the title of the panel). The distribution of differences and their significance values show no systematic trend in the colour-magnitude plane. Note that the best-fit HD is smoother than the mock HD distribution due to the oversampling of the model.

Test B produced similar results as test A, with star counts differences in the range [-2.69%, +2.49%]. The cell with the largest absolute difference (-2.69%) exhibits one bin in the HD diagram with maximum significance of 2.7σ. There is a general concordance in the remaining cells, with typical maximum significance $\leqslant 4\sigma$ in the cells of the HDs.

The differences between the recovered and true values (the last two columns of Table 2) are expected to follow a standard normal distribution, with μ=0 and σ=1. However, those values appear to be somewhat higher than expected, reflecting a systematic error in recover the true model greater than the uncertainty reported by the MCMC method. In order to encompass half of the recovery errors within $\pm0.67\sigma$ (or 50% of the area of the standard normal distribution), the uncertainties provided by EMCEE method are augmented by a factor of 3.0. In this way, we are aiming to inform realistic systematic errors in recovering the true model, and we are assuming they are calculated as those provided by EMCEE method scaled up to that factor.

3 DES DATA

The Dark Energy Survey (DES, DES Collaboration 2005) is a wide-area photometric survey covering about 5 000 deg^2 around the southern Galactic cap. DES images were taken with the Dark Energy Camera (DECam, Flaugher et al. 2015), with a typical single-exposure (90s in *griz* bands and 45s in Y band) 10σ limiting magnitudes of g = 23.57, r = 23.34, i = 22.78, z = 22.10 and Y = 20.69 for point sources (Morganson et al. 2018). The final coadded images at the end of the first 3 years of observations achieve g = 24.33, r = 24.08, i = 23.44, z = 22.69 and Y = 21.44 at S/N = 10 (DES Collaboration 2018). DES was designed for cosmological analyses, avoiding the Galactic plane (DES Collaboration 2018). Therefore, also considering the depth of the survey, the DES stellar sample will mostly contain stars from the Galactic thick disk and halo. In this section, we characterize the main aspects of the photometry and star/galaxy (S/G) separation in the DES.

DES-Y3 data was processed by the DES Data Management system (DESDM, Morganson et al. 2018) and includes observations from the first three years of the survey. The DES catalog applied here is the Year 3 Gold release version 2.2 (Sevilla-Noarbe, in preparation), hereafter refered as DES-Y3 catalogue. This catalog presents the same objects as the first public data release (DES-DR1; see DES Collaboration 2018), but contains enhanced photometric and morphological measurements and other ancillary information.

In order to identify the area covered by the DECam observations, the sky is partitioned in HEALPIX pixels (NSIDE=4096) with size equal to 52 arcsec × 52 arcsec (footprint map). Regions around stars brighter than J = 12 in 2MASS (Skrutskie et al. 2006), globular clusters (Harris 1996, updated 2010) and a small area close to Large Magellanic Cloud (LMC) were masked. The area covered by

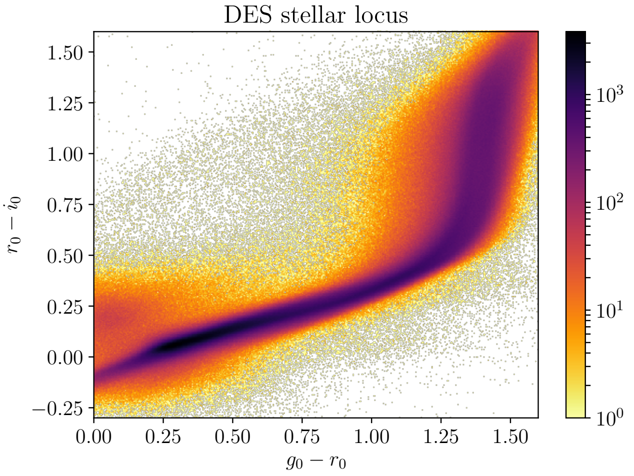

Figure 2. Colour-colour diagram showing the sources selected as stars in DES-Y3 Gold catalogue, following the selection described in the text and corrected for interestellar extinction.

DECam in each band and pixel (coverage map) is also estimated by a coverage map produced from `mangle` (Swanson et al. 2008). The DES-Y3 catalogue lists objects located in pixels (with NSIDE=4096) with sampled area $> 50\%$ in g, r, i and z bands and imaged at least once in all those four filters.

The DES-Y3 Gold data is photometrically calibrated by the Forward Global Calibration Method (FGCM[6], see Burke et al. 2018). A comparison between DES-Y3 and *Gaia* DR1 (Lindegren et al. 2016) shows a mean difference of 0.0014 magnitudes with $\sigma = 0.0067$ magnitudes (DES Collaboration 2018). The PSF photometry for DES-Y3 catalogue was performed by simultaneously fitting each object in multiple exposures (single object fitting or SOF). This procedure is very similar to the multi-object PSF-fitting (MOF) described in Drlica-Wagner et al. (2018).

We apply a S/G separation procedure that is similar to Shipp et al. (2018). We use the parameter `EXTEND_CLASS_MASH_SOF`, which is a variable designed to classify point source (star or quasi-stellar objects - QSO) or extended sources (galaxies) based on `ngmix` (Sheldon 2015). We nominally adopt values from the *single object fitting* photometry and when missing SOF photometry we adopt photometry from the coadded images. This criteria increases the stellar sample by including stars with good PSF-fitting in coadded images but with failures in SOF. This S/G separation is applied for objects in the full range of magnitudes. Similar to Shipp et al. (2018), the same weight-averaged `SPREAD_MODEL` in i band is applied as S/G classification for the small sample of bright stars ($g < 18$) where PSF photometry fails.

Extensive completeness assessments were carried out in the DES year 1 (DES-Y1) catalog, assuring that the catalogue is virtually complete in the range $17 < g < 22$, with estimated completeness $\geqslant 95\%$ at the faint limit (Sevilla-Noarbe et al. 2018). The authors of the latter work compare the DES-Y1 sample to Hyper Suprime-Cam DR1 (Aihara et al. 2018) data and estimate contamination by galaxies as $\leqslant 5\%$ in the same magnitude range. Similar completeness and contamination are found in DES-DR1 data (DES Collaboration 2018). Our sample is similar to the DES-DR1 sample, thus assuring the purity and completeness of the DES-Y3 data. We refer to the works above for a more detailed discussion about the quality of data, S/G separation, and other quantities involved.

The quality of the DES photometry and S/G classification is illustrated in Fig. 2, where we show a colour-colour diagram (g-r vs r-i) for sources classified as stars and corrected by reddening following Schlegel et al. (1998). There are 13,995,057 sources within the magnitude range $17 < g < 22$ and the limits shown in Fig. 2, namely $0.0 < g_0 - r_0 < 1.6$ and $-0.3 < r_0 - i_0 < 1.6$. A blue plume close to $g_0 - r_0 \cong 0$ and $r_0 - i_0 \cong 0.25$ amounts to a few thousands of stars, probably due to binary systems with a white dwarf and a main sequence star (Kleinman et al. 2004). A lower level of contamination by QSO's is expected in that region of the color-color diagram.

4 MWFITTING APPLIED TO DES-Y3 STARS

We partition the DES data into cells corresponding to HEALPIX pixels with NSIDE=16, covering a solid angle of 13.43 deg^2. The cells included in the analysis are those with a fill factor $\geqslant 80\%$ (> 10.74 deg^2) of its footprint. Such criterion (and others mentioned below) are identical to those adopted for the validation tests.

We choose a constant range of magnitude ($17 < g < 21$) and color ($0.0 < g - r < 0.8$) when applying the MWFITTING methodology to the DES data, following the discussion in Section 2.1. This constant color-magnitude selection is motivated by the uniformity of the DES footprint in this magnitude range, and we bin the data in color-magnitude space with a bin size of 0.1 mag in both color and magnitude. This choice of bin size is somewhat arbitrary, and we have found that the results of our analysis are insensitive to the choice of bin size.

The stars in our sample are not reddening corrected, instead the reddening is incorporated in the models following a Gaussian distribution based on the average and dispersion of the reddening on each cell.

Assuming that the components of the Galaxy are described by smooth profiles, we exclude cells with known stellar clusters and dwarf galaxies. The list of objects includes globular clusters and dwarf galaxies discovered up-to-date (Harris 1996, 2010 edition; McConnachie 2012; Drlica-Wagner et al. 2015; Koposov et al. 2015; Kim & Jerjen 2015; Luque et al. 2018), along with nearby galaxies partially resolved into stars in the DES images and catalogues (IC5152, ESO294-G010, NGC55, NGC300, NGC1399, NGC247, IC1613, ESO410-G005). The stars from those objects represent a potential contamination to Galactic fields and these fields contained positive residuals in initial iterations of MWFITTING.

Cells with any region closer than 22° from the LMC centre were also masked. Nidever et al. (2019) clearly shows (see their figure 5) significant amount of LMC main-sequence stars on regions located out to 21° from that galaxy. Furthermore, we masked the Sagittarius Stream, removing a

---

[6] `https://github.com/lsst/fgcmcal`

stripe of width equal to 20° along the centre of the stream (Majewski et al. 2003).

After removing the aforementioned regions and selecting only cells with a fill factor of more than 80%, the remaining 194 cells constitute our so-called *raw sample*. This sample includes the stellar population of streams discovered in the DES footprint (Shipp et al. 2018) and the Eridanus-Phenix overdensity (Eri-Phe, Li et al. 2016). Since these objects cover a large area with a much lower stellar density than that of the Galaxy, we retain them in the *raw sample*. However, a low level of contamination is expected.

4.1 With or without streams?

To explore the influence of including regions with known stellar streams and the Eri-Phe overdensity, we define a second sample removing the regions where those objects are located. The list of masked stellar streams is that described by Mateu (2017), and we refer to this work for further details. In the case of Eri-Phe over-density, the masked area has a triangular shape as shown in figure 3 of the discovery's paper. The second sample of DES data counts 105 cells, and we refer to this sample as the *refined sample*.

Figure 3 puts into perspective the footprint of *raw* and *refined* samples using an orthonormal projection of the southern Galactic Hemisphere. The DES footprint is outlined in black. The cells included in MWFITTING are displayed in green and masked cells are shown in orange. The *raw* and *refined* samples are top and bottom respectively. A significant portion of the DES footprint is masked in the *refined* sample.

The Sagittarius Stream (indicated in the Figure) stands out in both panels of Fig. 3 as a wide stripe crossing South Galactic Pole and cells masked due to proximity to the LMC are in the lower left corner. The area sampled by DES-Y3 and compared to models amounts to 2,315 deg^2 (194 cells) in the *raw* sample, and to 1,256 deg^2 (105 cells) in the *refined* sample.

4.2 MWFitting results

Before discussing the outcomes from the MWFITTING method to DES data, we first discuss the EMCEE configuration shared by both comparisons. We utilize 200 walkers along 250 steps with step length as 1% of each parameter to sample the posterior distribution. We perform an initialize iteration, starting with input values from the literature. In a second iteration, we redo the fit starting with outcomes from previous fitting. The first 150 steps are discarded as a burn-in phase, and we examine the remaining distribution to check that the walkers have converged. We apply a Gelman-Rubin convergence diagnostic ($R_c \leqslant 1.003$) to assure the convergence of the Markov chains of all the parameters.

The results of the MWFITTING method applied to *raw* and *refined* samples are listed in Table 3. We find that the errors reported from the posterior distribution are smaller than the difference of best-fit parameters when we tested the pipeline with subsets of the *raw* or *refined* sample. Hence, we have decided to assume the statistical errors from a *jackknife* resampling method (Feigelson and Babu 2012), in addition to the systematic errors based on the EMCEE method.

The *jackknife* method creates n samples (where n is the number of observations), replicating the initial sample in each iteration, but omitting the i-*th* observation. The *jackknife block* method is similar, but instead groups the observations into n_b data blocks with k size (in our case, the blocks are cells). In each subsample, a pseudo-value ps_i is calculated:

$$ps_i(X) = n_b\phi_n(X_1, ..., X_n) - (n_b - 1)\phi_{n-k}((X_1, ..., X_n)_{[i]}) \tag{2}$$

where ϕ_n is the statistical estimator (e. g. mean or dispersion) defined for n blocks and $\phi_{n-k}((X_1, ..., X_n)_{[i]}$ is the same estimator but for the *deleted-one* sample. The pseudo-values ps_i follow a standard normal distribution for the ϕ parameter with mean and standard deviation.

We adopted $k = 10$ for both samples, being $n_b = 20$ blocks in the *raw* and $n_b = 10$ blocks in *refined* sample. Following this method, the statistical errors indicated in Table 3 bound 1σ or 68% of the likelihood distribution of each parameter. A systematic error term is include to account for the ability of the pipeline to recover input values.

The best-fit parameters for the *raw* and *refined* samples agree within 1σ and have similar errors. The only exception is the error in the radial scale for the thick disk, but in both cases the best-fit values for this parameter agree very well with each other.

There is general agreement between our results and previous works (see Table 3), even through our uncertainties are substantially smaller. The best-fit parameters of the stellar halo agree reasonably well, except for the local stellar density. This disagreement may be related to different methods of estimating the total stellar mass, since different IMFs heavily influence the number of low-mass stars, most of which are not sampled by the HDs. Different approaches in selecting stars also impact the estimation of the total stellar mass. Likewise, we point out there is a discrepancy by a factor of $\sim$2 regarding the local halo stellar density between the estimations of Jurić et al. (2008) and de Jong et al. (2010). A similar result is achieved for the thick disk, which two parameters concur to the literature: the vertical scale and the density normalization, are within 1σ of the estimation from de Jong et al. (2010). The most significant disagreement occurs for the thick disk radial scale, which in our results is smaller than in both previous works. In spite of that, our best-fit model for the radial scale of the thick disk shows a striking similarity to that of Bovy et al. 2016 (2.2 ± 0.2 kpc), who fitted an exponential disk for mono abundance population of enhanced [α/Fe] APOGEE stars, a method utterly different from the one exhibited here.

5 SIMULATING THE STELLAR CONTENTS OF DES-Y3

With the best-fit parameters, we produce a simulated stellar DES-Y3 Gold catalogue to the limiting magnitude of $g = 24$ in the colour range $0 < g - r < 0.8$. These simulations will be compared to the entire footprint to analyze the stellar distribution of the catalogue, highlight asymmetries in the Galactic components (such as flares and warps in the disk), and potentially reveal stellar substructures. The

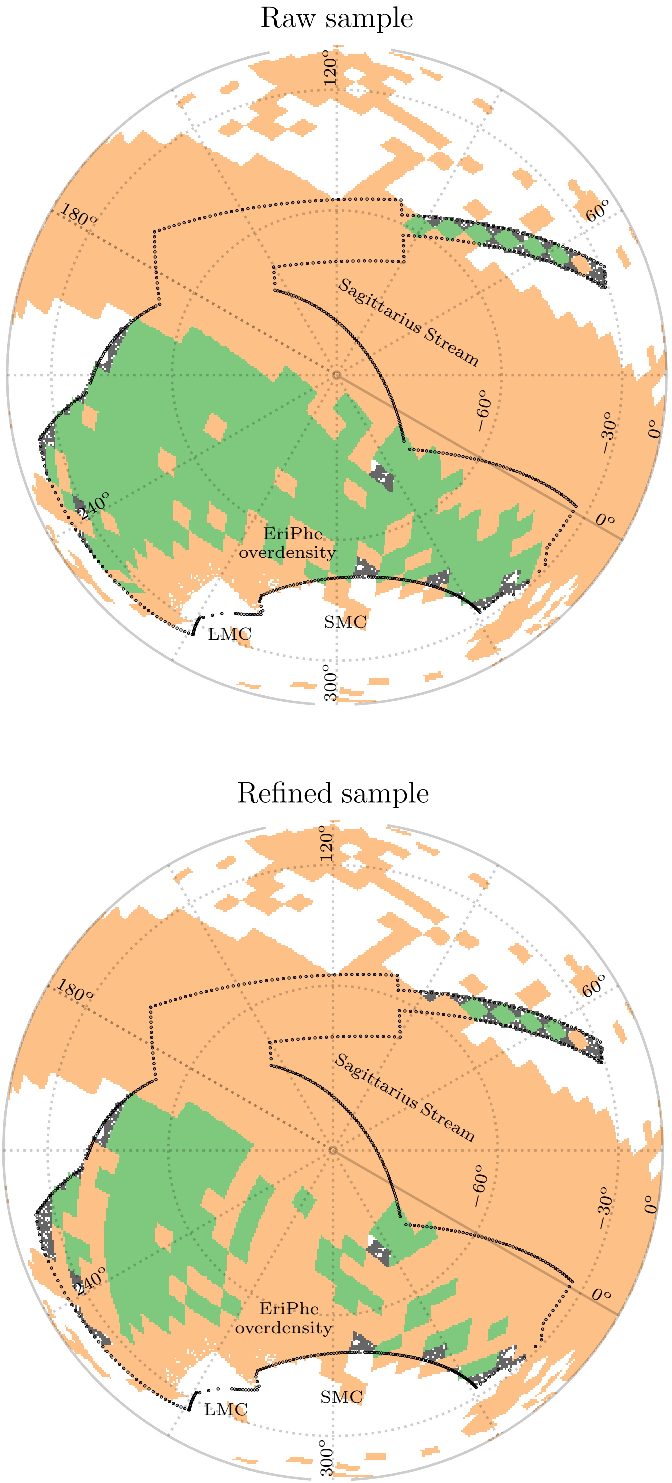

Figure 3. Galactic coordinates in an orthonormal projection showing the DES footprint (outlined by black dots) in the southern Galactic Hemisphere. The *raw sample* (*top*) and the *refined sample* (*bottom*) are shown as green diamonds. Cells in orange are masked, due to prominent stellar over-densities such as: globular clusters, dwarf galaxies, the Sagittarius Stream, the outskirts of the LMC and SMC, Eridanus-Phenix overdensity and stellar streams. LMC and SMC positions are indicated in the figure.

Table 3. Best-fit parameters for the *raw* and *refined* samples. The last two columns are results from the literature. In our results, the first errors listed are the 1σ statistical error or the standard deviation of the mean estimated by the *jackknife block* method (see more details in the text). The second errors are the systematic errors as discussed in Section 5, and they represent the ability of the pipeline to recover the true model.

Parameter	*Unit*	MWFITTING		Jurić et al. 2008	de Jong et al. 2010
		Raw sample	*Refined sample*		
ThickDisk h_e	pc	$819.0 \pm 7.0 \pm 5.4$	$824.0 \pm 7.0 \pm 5.4$	743 ± 150	750 ± 70
ThickDisk R_e	pc	$2293 \pm 32 \pm 22$	$2284 \pm 166 \pm 22$	3261 ± 650	4100 ± 400
ThickDisk ρ (R=R$_\odot$)	$\times10^{-3}$ M$_\odot$pc^{-2}	$4.16 \pm 0.10 \pm 0.12$	$4.02 \pm 0.15 \pm 0.12$	7.53 ± 0.75	5.01 ± 1.30
Halo n	-	$2.590 \pm 0.025 \pm 0.018$	$2.625 \pm 0.026 \pm 0.018$	2.77 ± 0.02	2.75 ± 0.07
Halo q	-	$0.637 \pm 0.009 \pm 0.009$	$0.618 \pm 0.014 \pm 0.009$	0.64 ± 0.01	0.88 ± 0.03
Halo ρ (R=R$_\odot$)	$\times10^{-5}$M$_\odot$pc^{-3}	$5.25 \pm 0.10 \pm 0.12$	$5.54 \pm 0.12 \pm 0.12$	2.95 ± 0.74	6.31 ± 0.77

histogram of the abundance of stars as function of g magnitude in DES-Y3 catalogue and simulations from several models are indicated in Fig. 4. The distribution of stars in the DES-Y3 data is shown as a blue line, while the distribution of stars in the simulation using the best-fit parameters from the *raw* and *refined* samples are shown as thick and thin green lines respectively. In addition, the predictions of the stellar distribution with two different distances for the *ad hoc* break in the power law index of the halo density profile at 27 and 43 kpc are illustrated by the red and cyan lines respectively. These predictions are based with the best-fit outcomes from the *raw* sample, as the results are alike for both samples. To demonstrate the key role of the halo, we produce a simulation of with the halo reduced to 80% of the best-fit value from the *raw*. The distribution of stars in that model is shown as a grey line (referred to as 'Halo model B') in Fig. 4.

The break power law model we use is from Deason et al. (2011). The power law indices drop from 2.59 (our best-fit value from the *raw* sample) to 4.6 (Deason et al. 2011). This model creates a smooth transition between the two density regimes.

The DES-Y3 Gold data is displayed as blue dots in Fig. 4. We have applied a completeness and contamination model following Shipp et al. 2018 (see their fig. 1).

An initial look at Fig. 4 reveals a pronounced increase in the sample of DES-Y3 stars between $23 < g < 24$, a behaviour absent in the simulated star counts. This effect is caused by the S/G separation, as the classifier's efficiency drops significantly near the limiting magnitude of the catalogue. Similar to the discussion in Sevilla-Noarbe et al. (2018) considering DES-Y1 data, the stellar sample in DES-Y3 Gold should also be strongly affected by the S/G classification at fainter magnitudes. We correlate this upturn in the DES-Y3 star counts fainter than $g = 23$ with a systematic galaxy contamination, since the appearance of QSO's in the stellar sample is expected at that magnitude level.

Concerning the stars brighter than $g = 23$, there is an interplay between the S/G classification and the completeness of the stellar sample. DES-Y3 sources are well classified up to $g \sim 22$, as mentioned by Sevilla-Noarbe et al. (2018) for the DES-Y1 data. However, the star counts present a maximum around $g = 21.5$, following a nearly flat region, and a valley close to $g \sim 23.0$, just before the sharp increase discussed in the previous paragraph.

The differences in the distribution of stars between the Halo Model B and the best-fit model for the *raw* sample slowly increase between $17 < g < 21$, while in the range $21 < g < 24$ they stand roughly steady in the logarithmic scale, implying that the ratio of stars between those two models is constant. This comparison demonstrates that decreasing only the normalised density of the halo does not improve the agreement between the observed data (blue dots) and the model (thick green line), as is expected. In this case, the behaviour of the DES-Y3 catalogue is not reproduced with a simple decrease in the halo density, attesting the reliability of the MWFITTING method. On the other hand, the effect of inserting a break in the power law promotes a better fit to the DES-Y3 catalogue, as we can see by the comparison between the DES-Y3 catalogue corrected by completeness and contamination (blue dots) and the model with a break at 27 kpc (red line).

Figure 4 shows a large level of consistency between the two best-fit models, both indicated by green lines. The differences in terms of star counts between both models is $\sim 10\%$ for fainter magnitudes ($g > 21$). While the best-fit parameters of the *refined* sample indicates a halo more dense at the Solar region than that model fit with the *raw* sample, the (absolute value of) halo's power law exponent increases and overall star counts decreases in the best-fit model for *refined sample* compared to the *raw* sample.

Figure 5 also explores the distribution of stars, but in the CMD space. This presents further evidence for that the break in the Galactic halo is preferred over no break. The first panel in Fig. 5 shows the CMD distribution of DES-Y3 stars, taking into account completeness and contamination, similar to the blue circles in Fig. 4. Analogous to the observed magnitude distribution at the faint end in Fig. 4, the

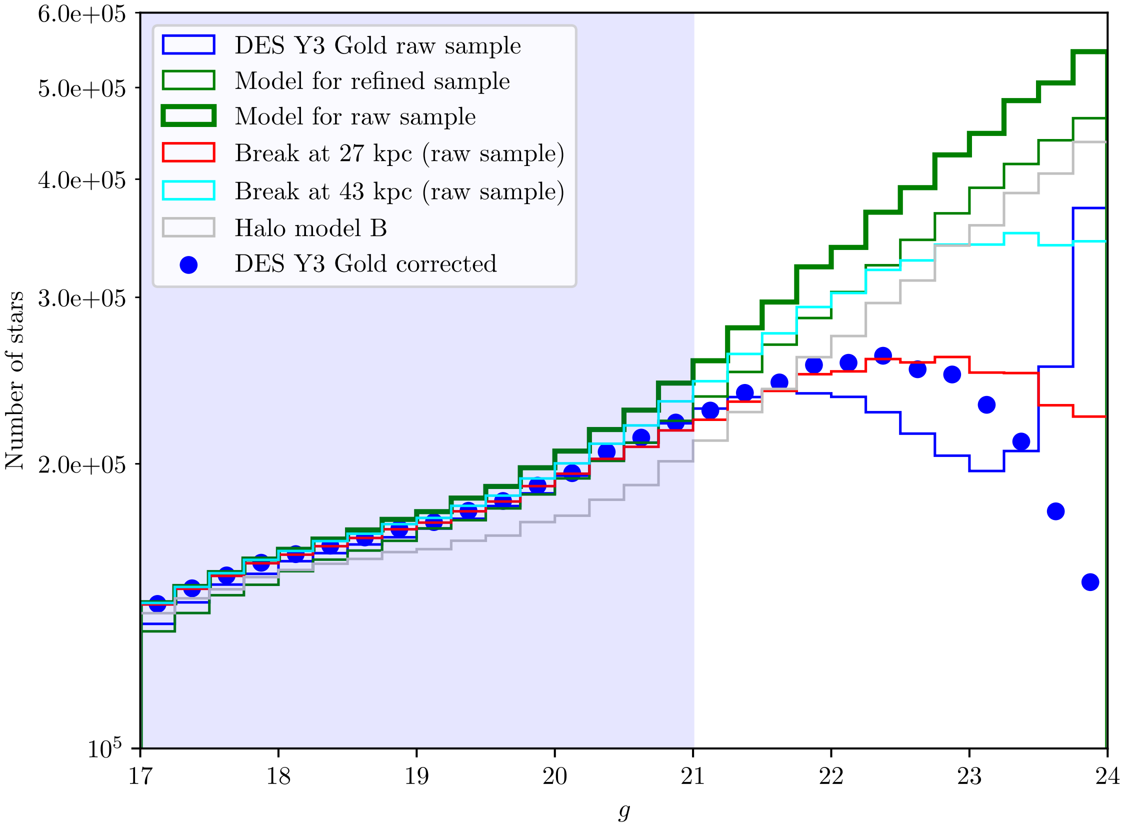

Figure 4. Stellar number distribution in g-band magnitude for the DES-Y3 catalog (blue lines), DES-Y3 catalog corrected for completeness and galaxy contamination (blue dots), and several different models (histograms). The models with their best-fit parameters displayed are: the *raw* sample (thick green line) and *refined* sample (thin green line) with a single power law, the *raw* sample with a break in the power law index at 27 kpc (red line) and 43 kpc (cyan line), and a model where the halo normalization has been decreased 80% to show how changes in the normalization affect the distribution (grey line). The blue shadow region defines the magnitude range used in MWFITTING. At faint magnitudes galaxies are leaking into the sample.

fainter end of the first panel in Fig. 5 shows a large number of sources, likely QSOs. The modelled stars are distributed in the second panel of Fig. 5 following the best-fit model for *raw* sample, with a break in the power law index at 27 kpc (similar to the red line in Fig. 4). Finally, the last panel shows the CMD of simulated stars without a break in the halo, leading to a steady increase of the number of stars at the faint end and being at odds with the data.

The first two panels of Fig. 5 exhibit strong similarities, at least for $g \lesssim 23$. The thick disk leaves its main imprint by the plume of MSTO stars at $g < 19$ and $g - r \simeq 0.4$. There is a smooth transition between the crowding of MSTO stars of the thick disk and the MSTO stars of the halo, which starts at $g \simeq 19$ but in a bluer region. This transition is seen in the Fig. 4 as a distribution of stars slightly more flat $(18 < g < 19)$ than the preceding or subsequent range. The MSTO stars of the halo are concentrated in a large range of magnitudes centered at $g \simeq 21$, whose density smoothly decreases towards the fainter end, which indicates a break in the halo.

Figs. 4 and 5 provides evidence to conclude that the break in the halo is required to correctly describe the stellar distribution beyond $g \simeq 21$. We also attest that the S/G classifier remains efficient (as evidenced by both star counts distributions and CMDs) down to $g \simeq 23$, even though fig. 11 of Sevilla-Noarbe et al. (2018) indicates some source confusion caused by the S/G separation for sources $g > 22$. The halo model with a power law break at 43 kpc is not efficient in decreasing the star counts for $g < 22$ compared to the model with a break in 27 kpc. Therefore, we may rule out such large radii for the break.

The estimation of star counts fainter than $g = 23$ is certainly important for future surveys such as the LSST (LSST Science Collaboration et al. 2009) and Euclid (Sartoris et al. 2016). For example, at $g = 24$, Fig. 4 shows that the expected number of halo stars with a break power law at 27 kpc is less than half the number from models with no break in the density power law index. Realistic simulations for future large and deep surveys must consider and account this feature of the halo at this depth. Since one of the major issues of large surveys is the S/G separation, an estimation of the star counts at a specific depth is important to evaluate the expected efficiency of the S/G classifier.

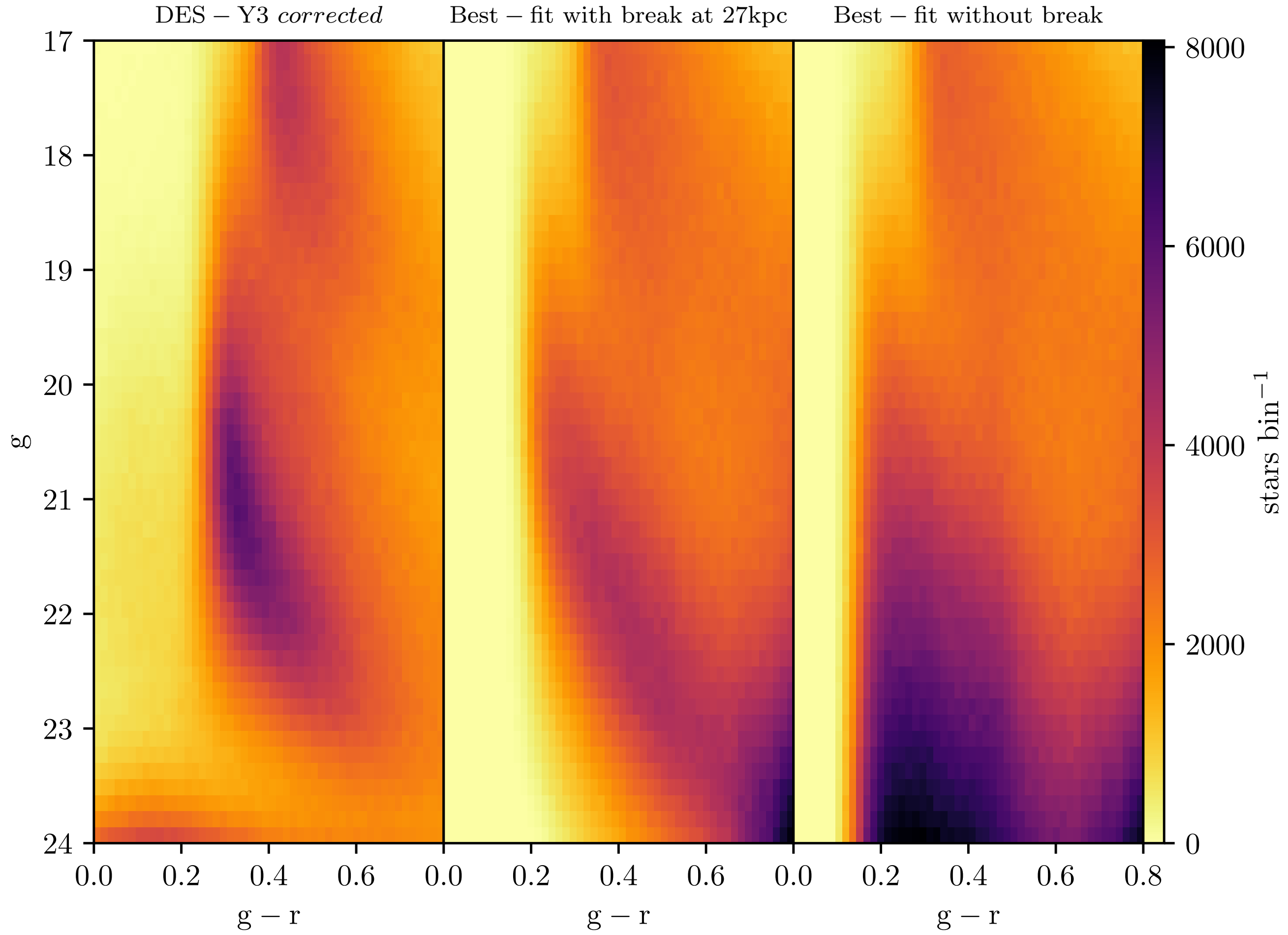

Figure 5. *Left panel:* CMD for DES-Y3 stars in the *raw* sample (blue circles in Fig. 4) corrected by completeness and contamination. *Central panel:* simulated CMD for the *raw* sample with the break in the halo density profile exponent at 27 kpc and (*right panel*) without any break in the halo exponent. The upturn in Fig. 4 in DES-Y3 close to $g = 23.5$, is understood as the contamination by QSO's. Note the agreement between the first and the second panel (with the exception of the QSO's in the fainter blue end of left panel and modelled red dwarfs in the red limit of the central panel.)

5.1 Poissonian significance maps

We show the Poissonan significance map for both samples of the DES-Y3 data in Fig. 6. The residuals are determined with the best-fit models after applying the power law break following Deason et al. (2011). In order to provide a more realistic comparison, the DES-Y3 catalogue in the Fig. 6 was corrected with the completeness and contamination curves following fig. 1 of Shipp et al. (2018).

The significance of each 7×7 arcmin^2 pixel is taken as the residual star counts (difference between the DES-Y3 catalog and the modelled catalog) divided by the square root of modelled star counts. After this step, both maps are smoothed with a Gaussian with $\sigma = 7$ arcmin. The minimum significance for both samples are roughly the same (-7.64 for *refined sample* and -7.57 for *raw sample*), but is shown in the same range in order to compare both maps within the same range of significance. Pixels with higher significance are saturated in the positive value of minimum value to highlight under/overdensities as blue/reddish colours, and white colour represents a perfect agreement between models and data. The lowest values for significance indicate small regions where the extinction is an outlier of the distribution of the extinction in the respective cell.

Many known Galactic substructures are enhanced, attesting the excellent job made by MWFITTING. Given the steep increase of stars at faint g-magnitudes in Fig. 4, we build up the maps only down to $g = 23.5$, avoiding fainter magnitudes where the S/G classification is not efficient. When extending the limit down to $g = 24$, the expected extra-galactic sources would pollute the map with cosmological large-scale structures.

We label the most significant stellar over-densities on both panels of Fig. 6. For instance, the stripe roughly parallel to $l = 180°$ is the Sagittarius Stream and the secondary branch is visible. The over-density associated with SMC (SMCNOD) in the anti-LMC side (Pieres et al. 2017;

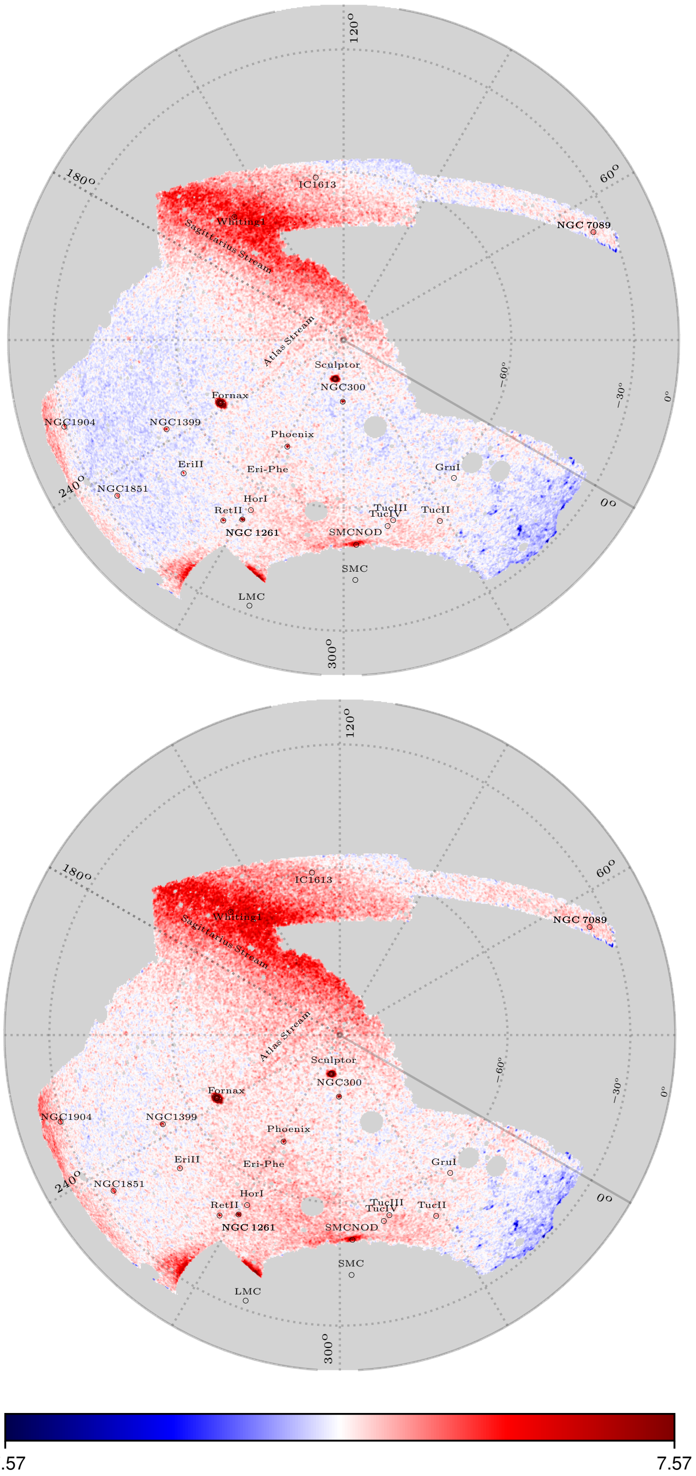

Figure 6. Smoothed Poisson significance of residual maps between the DES-Y3 stars and best fit MW models created with the *raw* (top) and *refined* (bottom) samples, with a limiting magnitude of $g = 23.5$. Both models include a break in the power law at 27 kpc where the exponent changes from the best-fit power law halo exponent to 4.6, smoothed using a Gaussian kernel with full-width-half-maxima $\simeq 16$ arcmin. Many over-densities are identified, most of them are associated with known objects including globular clusters, dwarf galaxies and stellar streams (including Sagittarius Stream, roughly parallel to $l = 180°$). Both maps are set to the same scale. Despite the fact that we are not fitting the thin disk, the overall significance across the footprint is close to zero, except in the region $\theta \sim -30°$, $\phi \sim 345°$, where there are hints that the bulge model could be improved. Regions masked (not covered by DES or close to bright stars) are shown in gray.

Mackey et al. 2018) is also evident. Although we are not using a *matched filter* (see e. g. Odenkirchen et al. 2003), a technique commonly applied to highlight fainter substructures as streams, a few streams are noticeable or suggested in Fig. 6. The Atlas stream (Koposov et al. 2014; Shipp et al. 2018), a subtle track of stars close to Galactic Pole (indicated in Fig. 6), is a good example of such structures.

The regions at the lowest Galactic latitudes between $240^\circ < l < 270^\circ$ presents smooth and flat over-densities (with the exception of the region close to LMC) in both panels of Fig. 6, which may indicate that there is room for improvement in the thin disk model. The region at $b < -30^\circ$, $220^\circ < l < 240^\circ$ in DES-Y3 footprint exhibits a strong excess of stars close to NGC1904, which may be the result of disk flaring or the Southern extension of the Monoceros Ring (Newberg et al. 2002).

The Eridanus-Phoenix over-density (Li et al. 2016) is seen as a very large over-density of stars between $270^\circ < l < 330^\circ$ and $-40^\circ < b < -70^\circ$, populating a triangle with vertices close of LMC, SMC and Fornax dwarf galaxy. The limits of the Eridanus-Phoenix over-density are more clearly defined in the top panel of Fig. 6, but on both panels an extension of stars towards the Galactic centre is suggested (possibly related to the Eridanus-Phoenix over-density). Subtracting the stars in the modelled catalog, the Eridanus-Phoenix cloud contains an over-density of 13262 (7810) stars within the range ($17 < g < 22$ and $0.0 < g - r < 0.8$) when compared to the best-fit of the *raw* (*refined*) sample. Accounting for stars more massive than 0.1 $M_\odot$ in a Chabrier mass function (Chabrier et al. 2000) for a disk-like IMF stars, those values correspond to an object with $\simeq 4.6 \times 10^4$ ($\simeq 2.8 \times 10^4$) $M_\odot$ for the *raw* (*refined*) sample. These mass estimations represent a decrease in mass of at least by factor of two compared to the estimates in Li et al. (2016).

The entire set of stellar streams listed in Shipp et al. (2018) is detected in the subtracted (data minus simulated catalogue) density maps when a *matched filter* technique is applied to DES-Y3 catalogue to select main sequence stars. In addition to that list, the Corvus Stream (Mateu et al. 2018) is detected in the eastern extreme of the footprint.

A noticeable feature is an excess of simulated stars at lower Galactic latitude close to the bulge, which may indicate that our assumptions in the bulge model should be revisited. Alternatively, it may reflect a different extinction law towards these directions than the one we adopted here (see Nataf et al. 2013). Those differences indicated by the significance map in the bulge extends as far as ∼40° (or 5.6 kpc) from the Galactic Centre.

Even though the MW parameters for both samples agree within 1σ, there are relevant differences regarding the two panels of Fig 6. As the *raw* sample incorporates a few stars from overdensities, the best-fit parameters are somewhat shifted compared to the *refined* sample towards higher densities. This can be seen in Fig. 4 where the simulation with the best-fit *raw* sample parameters indicates a Galaxy more massive than predicted with the *refined* sample. Hence, the significance map on the top panel of Fig. 6 seems to narrow the limits of a few objects, as the Eridanus-Phoenix over-density and Sagittarius Stream. That shift is borne out by the higher significances for the stellar over-densities in the *refined* sample (bottom panel of Fig 6).

Table 4. Stellar masses estimates for the MW components fit in this work, for the *raw* and *refined* samples. The estimates for the halo stellar mass assume a break in the power law index at 27 kpc following the model detailed in the text.

Component	Estimated mass ($M_\odot$)	
	Raw sample	*Refined sample*
Thick disk	$6.04 \pm 0.31 \times 10^6$	$5.88 \pm 1.20 \times 10^6$
Halo (d<27kpc)	$4.12 \pm 0.24 \times 10^8$	$4.36 \pm 0.10 \times 10^8$
Halo (d>27kpc)	$2.54 \pm 0.16 \times 10^6$	$2.71 \pm 0.08 \times 10^6$
Halo (total)	$4.15 \pm 0.24 \times 10^8$	$4.38 \pm 0.10 \times 10^8$

5.2 Milky Way stellar mass

We calculate the stellar masses of the halo and thick disk MW components with the best-fit parameters (Table 3) and list them in Table 4. These mass estimations only include field stars following from a smooth model for the Galactic components, and therefore exclude the mass from globular clusters, dwarf galaxies, and streams.

The bulge parameters are kept fixed, and the model described in Table 1 amounts to a stellar mass of 1.28×10^{10} $M_\odot$ or 18.2% of the total stellar mass of the Galaxy. This agrees with mass estimates from the literature, where estimates of the stellar bulge mass range from 10-20% of the MW stellar mass (Licquia & Newman 2015; Portail et al. 2017). Our model include a thin disk (with fixed parameters) and has a stellar mass of 5.65×10^{10} $M_\odot$, which is within 1σ (68%) of the estimation by Licquia & Newman 2015 ($5.17 \pm 1.11 \times 10^{10}$ $M_\odot$). The ratio of stellar mass in the thin and thick stellar disks is $\cong 9\,200$. The thick disk has a small contribution to total disk mass.

The halo mass is estimated adding all halo stars farther than 1 kpc from the Galactic Centre, avoiding high densities given by power law in the central region dominated by Galactic bulge. For both samples, most of the stellar halo mass (> 99%) is within 27 kpc, where the break in the halo power law slope is roughly expected to be. In face of the numbers presented here, the stellar halo mass has a contribution of merely 0.6% of the Galactic stellar mass, whereas the disks contribute with 80.8% of the total.

Combining all the stellar components of the MW (thin and thick disks, bulge and halo), we obtain a total stellar mass of $7.03 \pm 1.05 \times 10^{10}$ $M_\odot$, with the best-fit parameters for both samples. The error is estimated following the uncertainties in the thin disk and bulge models, even those components are keep fixed in the fitting. Our MW stellar mass estimation agrees with Licquia & Newman (2015), where they determined the MW stellar mass (bulge, bar and disks) as $6.08 \pm 1.14 \times 10^{10}$ $M_\odot$, using a compilation of measurements. McMillan (2011) also applied a similar approach to photometric and kinematic data, with similar results ($6.43 \pm 0.63 \times 10^{10}$ $M_\odot$).

6 CONCLUDING REMARKS

We have developed a new code to fit the stellar components of the MW. In this first paper, we concentrate on fitting the thick disk and the halo due to the limited coverage of the DES footprint. We list our main conclusions from this work.

- This work presents MWFITTING, a pipeline constructed to fit structural parameters for the Galactic components with TRILEGAL stellar population synthesis models.
- The MWFITTINGpipeline is validated with synthetic catalogs. We successfully recovered the input parameters (with a maximum deviation of $\leqslant 3\%$) using the same oversampling factor and a footprint smaller than the real data (see Table 2).
- Our main goal in this work is to model the halo and the thick disk components by applying the MWFITTING pipeline to data from DES-Y3 Gold catalogue. We defined two different samples based on known stellar over-densities. Both samples excluded cells populated by dwarf galaxies, globular clusters and cells close to the LMC. In the *refined* sample, we further excluded cells where stellar streams and Eridanus-Phoenix over-density are located.
- Table 3 lists the results for both samples, with uncertainties determined by *jackknife* resampling and the EMCEE method. Results from both samples agree within a confidence level of 68% (1σ).
- The distribution of DES-Y3 stars, corrected by completeness and contamination, presents a very good agreement with our models when a break in the power law index in the halo density profile at $\simeq 27$ kpc is applied, down to $g = 23$. Fainter than that magnitude, there is an increase of point-like sources towards the fainter end ($g = 24$), that we interpret as a misclassification of galaxies as stars. Within the range $17 < g < 23$, the observed counts are compatible with the same broken power law halo model detailed in the text.
- CMDs comparing DES-Y3 stars and simulations agree remarkably well up to $g = 23$, beyond which misclassification becomes important. The CMD for the model with a single halo power law shows a steady increase of sources not seen in the data.
- Simulations over the entire DES-Y3 footprint based on our best-fitting models were produced. Both samples present a remarkable agreement to the data. Residual maps highlight many over-densities associated with globular clusters, dwarf galaxies, clouds, and streams in the DES footprint.
- Integrating the MW components with the best-fit model (bulge, thin and thick disk, and halo) leads us to estimate the total stellar mass of the Galaxy as $7.03 \pm 1.05 \times 10^{10}$ $M_{\odot}$. This result agrees with previous works, such as Licquia & Newman 2015 ($6.08 \pm 1.14 \times 10^{10}$ $M_{\odot}$) and McMillan 2011 ($6.43 \pm 0.63 \times 10^{10}$ $M_{\odot}$).
- Simulations show there is a significant difference in the amount of faint stars ($g > 21$) between models with and without a break in the halo power law. Determining this break in the stellar halo is crucial in predicting the density of stars at faint magnitudes, which will be sampled in future surveys such as, the LSST or Euclid.

Future work with MWFITTING will include data from other wide-field surveys to extend the analysis to both the North and South Galactic Hemispheres and will include improvements to the modeling for the Galactic halo (e.g., tri-axial model).

ACKNOWLEDGEMENTS

Funding for the DES Projects has been provided by the U.S. Department of Energy, the U.S. National Science Foundation, the Ministry of Science and Education of Spain, the Science and Technology Facilities Council of the United Kingdom, the Higher Education Funding Council for England, the National Center for Supercomputing Applications at the University of Illinois at Urbana-Champaign, the Kavli Institute of Cosmological Physics at the University of Chicago, the Center for Cosmology and Astro-Particle Physics at the Ohio State University, the Mitchell Institute for Fundamental Physics and Astronomy at Texas A&M University, Financiadora de Estudos e Projetos, Fundação Carlos Chagas Filho de Amparo à Pesquisa do Estado do Rio de Janeiro, Conselho Nacional de Desenvolvimento Científico e Tecnológico and the Ministério da Ciência, Tecnologia e Inovação, the Deutsche Forschungsgemeinschaft and the Collaborating Institutions in the Dark Energy Survey.

The Collaborating Institutions are Argonne National Laboratory, the University of California at Santa Cruz, the University of Cambridge, Centro de Investigaciones Energéticas, Medioambientales y Tecnológicas-Madrid, the University of Chicago, University College London, the DES-Brazil Consortium, the University of Edinburgh, the Eidgenössische Technische Hochschule (ETH) Zürich, Fermi National Accelerator Laboratory, the University of Illinois at Urbana-Champaign, the Institut de Ciències de l'Espai (IEEC/CSIC), the Institut de Física d'Altes Energies, Lawrence Berkeley National Laboratory, the Ludwig-Maximilians Universität München and the associated Excellence Cluster Universe, the University of Michigan, the National Optical Astronomy Observatory, the University of Nottingham, The Ohio State University, the University of Pennsylvania, the University of Portsmouth, SLAC National Accelerator Laboratory, Stanford University, the University of Sussex, Texas A&M University, and the OzDES Membership Consortium.

Based in part on observations at Cerro Tololo Inter-American Observatory, National Optical Astronomy Observatory, which is operated by the Association of Universities for Research in Astronomy (AURA) under a cooperative agreement with the National Science Foundation.

The DES data management system is supported by the National Science Foundation under Grant Numbers AST-1138766 and AST-1536171. The DES participants from Spanish institutions are partially supported by MINECO under grants AYA2015-71825, ESP2015-66861, FPA2015-68048, SEV-2016-0588, SEV-2016-0597, and MDM-2015-0509, some of which include ERDF funds from the European Union. IFAE is partially funded by the CERCA program of the Generalitat de Catalunya. Research leading to these results has received funding from the European Research Council under the European Union's Seventh Framework Program (FP7/2007-2013) including ERC grant agreements 240672, 291329, and 306478. We acknowledge support from the Australian Research Council Centre of Excellence for All-sky Astrophysics (CAASTRO), through project number CE110001020, and the Brazilian Instituto Nacional de Ciência e Tecnologia (INCT) e-Universe (CNPq grant 465376/2014-2).

This manuscript has been authored by Fermi Research Alliance, LLC under Contract No. DE-AC02-07CH11359 with the U.S. Department of Energy, Office of Science, Office of High Energy Physics. The United States Government retains and the publisher, by accepting the article for publication, acknowledges that the United States Government retains a non-exclusive, paid-up, irrevocable, worldwide license to publish or reproduce the published form of this manuscript, or allow others to do so, for United States Government purposes.

References

Abbott, T. M. C., Abdalla, F. B., Allam, S., et al. 2018, Astrophysical Journal Supplement Series, 239, 18

Aihara, H., Armstrong, R., Bickerton, S., et al. 2018, Publications of the Astronomical Society of Japan, 70, S8

Anders, F., Chiappini, C., Santiago, B. X., et al. 2014, Astronomy & Astrophysics, 564, A115

Arnouts, S., Vandame, B., Benoist, C., et al. 2001, Astronomy & Astrophysics, 379, 740

Balbinot, E., Santiago, B. X., Girardi, L., et al. 2015, Monthly Notices of the Royal Astronomical Society, 449, 1129

Bahcall, J. N., & Soneira, R. M. 1981, Astrophysical Journal Supplement Series, 47, 357

Bechtol, K., Drlica-Wagner, A., Balbinot, E., et al. 2015, The Astrophysical Journal, 807, 50

Bensby, T., Feltzing, S., & Lundström, I. 2003, Astronomy & Astrophysics, 410, 527

Bensby, T., & Feltzing, S. 2010, Chemical Abundances in the Universe: Connecting First Stars to Planets, 265, 300

Bernard, E. J., Ferguson, A. M. N., Schlafly, E. F., et al. 2016, Monthly Notices of the Royal Astronomical Society, 463, 1759

Bertelli, G., Bressan, A., Chiosi, C., Fagotto, F., & Nasi, E. 1994, A&AS, 106, 275

Binney, J., Gerhard, O., & Spergel, D. 1997, Monthly Notices of the Royal Astronomical Society, 288, 365

Binney, J., & Tremaine, S. 2008, Galactic Dynamics: Second Edition, by James Binney and Scott Tremaine. ISBN 978-0-691-13026-2 (HB). Published by Princeton University Press, Princeton, NJ USA, 2008.,

Bland-Hawthorn, J., & Gerhard, O. 2016, ARA&A, 54, 529

Blanton, M. R., Bershady, M. A., Abolfathi, B., et al. 2017, The Astronomical Journal, 154, 28

Boeche, C., Siebert, A., Piffl, T., et al. 2013, Astronomy & Astrophysics, 559, A59

Bournaud, F., Elmegreen, B. G., & Martig, M. 2009, The Astrophysical Journal Letters, 707, L1

Bovy, J., Rix, H.-W., Schlafly, E. F., et al. 2016, The Astrophysical Journal, 823, 30

Brook, C. B., Kawata, D., Gibson, B. K., & Freeman, K. C. 2004, The Astrophysical Journal, 612, 894

Burke, D. L., Rykoff, E. S., Allam, S., et al. 2018, The Astronomical Journal, 155, 41

Cabrera-Lavers, A., Garzón, F., & Hammersley, P. L. 2005, Astronomy & Astrophysics, 433, 173

Chabrier, G., Baraffe, I., Allard, F., & Hauschildt, P. 2000, The Astrophysical Journal, 542, 464

Chabrier, G. 2003, Publications of the Astronomical Society of the Pacific, 115, 763

Chiba, M., & Beers, T. C. 2000, The Astronomical Journal, 119, 2843

Courteau, S., Widrow, L. M., McDonald, M., et al. 2011, The Astrophysical Journal, 739, 20

Czekaj, M. A., Robin, A. C., Figueras, F., Luri, X., & Haywood, M. 2014, Astronomy & Astrophysics, 564, A102

de Jong, J. T. A., Yanny, B., Rix, H.-W., et al. 2010, The Astrophysical Journal, 714, 663

Deason, A. J., Belokurov, V., & Evans, N. W. 2011, Monthly Notices of the Royal Astronomical Society, 416, 2903

Deason, A. J., Belokurov, V., & Koposov, S. E. 2018, The Astrophysical Journal, 852, 118

DES Collaboration 2005, ArXiv e-prints, arXiv:astro-ph/0510346

Desai, S., Armstrong, R., Mohr, J. J., et al. 2012, The Astrophysical Journal, 757, 83

Dolphin, A. E. 2002, Monthly Notices of the Royal Astronomical Society, 332, 91

Drlica-Wagner, A., Bechtol, K., Rykoff, E. S., et al. 2015, The Astrophysical Journal, 813, 109

Drlica-Wagner, A., Sevilla-Noarbe, I., Rykoff, E. S., et al. 2018, Astrophysical Journal Supplement Series, 235, 33

Eggen, O. J., Lynden-Bell, D., & Sandage, A. R. 1962, The Astrophysical Journal, 136, 748

Eidelman, S., Hayes, K. G., et al. 2004, Physics Letters B, 592, 1

Fausti Neto, A., da Costa, L. N., Carnero, A., et al. 2018, Astronomy and Computing, 24, 52

Feigelson, E. D., Babu, G. J. 2012, Modern Statistical Methods for Astronomy: With R Applications, by Eric D. Feigelson and G. Jogesh Babu. ISBN 978-1-139-53609-7 (HB). Published by Cambridge University Press, UK, 2012.

Flaugher, B., Diehl, H. T., Honscheid, K., et al. 2015, The Astronomical Journal, 150, 150

Fletcher, R. 1987, Practical methods of optimization, by Robert Fletcher. ISBN 978-0-471-91547-8 (HB). Published by Wiley, Hoboken, NJ USA, 1987.

Foreman-Mackey, D., Hogg, D. W., Lang, D., & Goodman, J. 2013, Publications of the Astronomical Society of the Pacific, 125, 306

Fuhrmann, K. 1998, Astronomy & Astrophysics, 338, 161

Fuhrmann, K. 2008, Monthly Notices of the Royal Astronomical Society, 384, 173

Gilmore, G., & Reid, N. 1983, Monthly Notices of the Royal Astronomical Society, 202, 1025

Girardi, L., Bressan, A., Bertelli, G., & Chiosi, C. 2000, A&AS, 141, 371

Girardi, L., Bertelli, G., Bressan, A., et al. 2002, Astronomy & Astrophysics, 391, 195

Girardi, L., Groenewegen, M. A. T., Hatziminaoglou, E., & da Costa, L. 2005, Astronomy & Astrophysics, 436, 895

Girardi, L., Williams, B. F., Gilbert, K. M., et al. 2010, The Astrophysical Journal, 724, 1030

Girardi, L., Barbieri, M., Groenewegen, M. A. T., et al. 2012, Astrophysics and Space Science Proceedings, 26, 165

Grillmair, C. J., & Dionatos, O. 2006, The Astrophysical Journal Letters, 643, L17

Groenewegen, M. A. T., Girardi, L., Hatziminaoglou, E., et al. 2002, Astronomy & Astrophysics, 392, 741

Gschwend, J., Rossel, A. C., Ogando, R. L. C., et al. 2018, Astronomy and Computing, 25, 58

Harris, W. E. 1996, The Astronomical Journal, 112, 1487

Helmi, A. 2016, The General Assembly of Galaxy Halos: Structure, Origin and Evolution, 317, 228

Helmi, A., Babusiaux, C., Koppelman, H. H., et al. 2018, Nature, 563, 85

Hopkins, P. F., Kereš, D., Oñorbe, J., et al. 2014, Monthly Notices of the Royal Astronomical Society, 445, 581

Jurić, M., Ivezić, Ž., Brooks, A., et al. 2008, The Astrophysical Journal, 673, 864

Lindegren, L., Lammers, U., Bastian, U., et al. 2016, Astronomy & Astrophysics, 595, A4

Kim, D., & Jerjen, H. 2015, The Astrophysical Journal Letters, 808, L39

Kleinman, S. J., Harris, H. C., Eisenstein, D. J., et al. 2004, The Astrophysical Journal, 607, 426

Koposov, S. E., Irwin, M., Belokurov, V., et al. 2014, Monthly Notices of the Royal Astronomical Society, 442, L85

Koposov, S. E., Belokurov, V., Torrealba, G., & Evans, N. W. 2015, The Astrophysical Journal, 805, 130

Kroupa, P., & Weidner, C. 2003, The Astrophysical Journal, 598, 1076

Kroupa, P. 2001, Monthly Notices of the Royal Astronomical Society, 322, 231

Li, T. S., Balbinot, E., Mondrik, N., et al. 2016, The Astrophysical Journal, 817, 135

Licquia, T., & Newman, J. 2013, American Astronomical Society Meeting Abstracts #221, 221, 254.11

Licquia, T. C., & Newman, J. A. 2015, The Astrophysical Journal, 806, 96

Loebman, S. R., Roškar, R., Debattista, V. P., et al. 2011, The Astrophysical Journal, 737, 8

LSST Science Collaboration, Abell, P. A., Allison, J., et al. 2009, arXiv:0912.0201

Luque, E., Santiago, B., Pieres, A., et al. 2018, Monthly Notices of the Royal Astronomical Society, 478, 2006

Lyngå, G. 1982, Astronomy & Astrophysics, 109, 213

Mackey, D., Koposov, S., Da Costa, G., et al. 2018, The Astrophysical Journal Letters, 858, L21

Maíz-Apellániz, J. 2001, The Astronomical Journal, 121, 2737

Majewski, S. R., Skrutskie, M. F., Weinberg, M. D., & Ostheimer, J. C. 2003, The Astrophysical Journal, 599, 1082

Majewski, S. R., APOGEE Team, & APOGEE-2 Team 2016, Astronomische Nachrichten, 337, 863

Marigo, P., & Girardi, L. 2007, Astronomy & Astrophysics, 469, 239

Marigo P., et al., 2017, The Astrophysical Journal, 835, 77

Mateu, C., Read, J. I., & Kawata, D. 2018, Monthly Notices of the Royal Astronomical Society, 474, 4112

Mateu, C. 2017, Astrophysics Source Code Library, ascl:1711.010

McConnachie, A. W. 2012, The Astronomical Journal, 144, 4

McMillan, P. J. 2011, Monthly Notices of the Royal Astronomical Society, 414, 2446

Minchev, I., Martig, M., Streich, D., et al. 2015, The Astrophysical Journal Letters, 804, L9

Morganson, E., Gruendl, R. A., Menanteau, F., et al. 2018, Publications of the Astronomical Society of the Pacific, 130, 074501

Mohr, J. J., Adams, D., Barkhouse, W., et al. 2008, Proceedings of Society of Photo-Optical Instrumentation Engineers, 7016, 70160L

Mohr, J. J., Armstrong, R., Bertin, E., et al. 2012, Proceedings of Society of Photo-Optical Instrumentation Engineers, 8451, 84510D

Nataf, D. M., Gould, A., Fouqué, P., et al. 2013, The Astrophysical Journal, 769, 88

Newberg, H. J., Yanny, B., Rockosi, C., et al. 2002, The Astrophysical Journal, 569, 245

Ngeow, C., Mohr, J. J., Alam, T., et al. 2006, Proceedings of Society of Photo-Optical Instrumentation Engineers, 6270, 627023

Nidever, D. L., Olsen, K., Choi, Y., et al. 2019, The Astrophysical Journal, 874, 118

Odenkirchen, M., Grebel, E. K., Dehnen, W., et al. 2003, The Astronomical Journal, 126, 2385

Osmer, P. S., Kennefick, J. D., Hall, P. B., & Green, R. F. 1998, Astrophysical Journal Supplement Series, 119, 189

Pasetto, S., Grebel, E. K., Chiosi, C., et al. 2018, The Astrophysical Journal, 860, 120

Paxton, B., Bildsten, L., Dotter, A., et al. 2011, Astrophysical Journal Supplement Series, 192, 3

Perryman, M. A. C., Lindegren, L., Kovalevsky, J., et al. 1997, Astronomy & Astrophysics, 323, L49

Pieres, A., Santiago, B. X., Drlica-Wagner, A., et al. 2017, Monthly Notices of the Royal Astronomical Society, 468, 1349

Portail, M., Gerhard, O., Wegg, C., & Ness, M. 2017, Monthly Notices of the Royal Astronomical Society, 465, 1621

Rana, N. C., & Basu, S. 1992, Astronomy & Astrophysics, 265, 499

Reddy, B. E., Lambert, D. L., & Allende Prieto, C. 2006, Monthly Notices of the Royal Astronomical Society, 367, 1329

Rocha-Pinto, H. J., Maciel, W. J., Scalo, J., & Flynn, C. 2000, Astronomy & Astrophysics, 358, 850

Ryan, S. G., & Norris, J. E. 1991, The Astronomical Journal, 101, 1865

Sarajedini, A., Bedin, L. R., Chaboyer, B., et al. 2007, The Astronomical Journal, 133, 1658

Sartoris, B., Biviano, A., Fedeli, C., et al. 2016, Monthly Notices of the Royal Astronomical Society, 459, 1764

Schlegel, D. J., Finkbeiner, D. P., & Davis, M. 1998, The Astrophysical Journal, 500, 525

Schönrich, R., & Binney, J. 2009, Monthly Notices of the Royal Astronomical Society, 396, 203

Sesar, B., Jurić, M., & Ivezić, Ž. 2011, The Astrophysical Journal, 731, 4

Sevilla, I., Armstrong, R., Bertin, E., et al. 2011, arXiv:1109.6741

Sevilla-Noarbe, I., Hoyle, B., Marchã, M. J., et al. 2018, Monthly Notices of the Royal Astronomical Society, 481, 5451

Sheldon, E. 2015, Astrophysics Source Code Library, ascl:1508.008

Skrutskie, M. F., Cutri, R. M., Stiening, R., et al. 2006, The Astronomical Journal, 131, 1163

Sharma, S., Bland-Hawthorn, J., Johnston, K. V., & Binney, J. 2011, The Astrophysical Journal, 730, 3

Shipp, N., Drlica-Wagner, A., Balbinot, E., & DES Collaboration 2018, American Astronomical Society Meeting Abstracts #231, 231, #212.05

Slater, C. T., Nidever, D. L., Munn, J. A., Bell, E. F., & Majewski, S. R. 2016, The Astrophysical Journal, 832, 206

Spada, F., Demarque, P., Kim, Y.-C., & Sills, A. 2013, The Astrophysical Journal, 776, 87

Steinmetz, M. 2012, Astronomische Nachrichten, 333, 523

Stoughton, C., Lupton, R. H., Bernardi, M., et al. 2002, The Astronomical Journal, 123, 485

Swanson, M. E. C., Tegmark, M., Hamilton, A. J. S., & Hill, J. C. 2008, Monthly Notices of the Royal Astronomical Society, 387, 1391

Torrealba, G., Catelan, M., Drake, A. J., et al. 2015, Monthly Notices of the Royal Astronomical Society, 446, 2251

VandenBerg, D. A., Bergbusch, P. A., & Dowler, P. D. 2006, Astrophysical Journal Supplement Series, 162, 375

Vanhollebeke, E., Groenewegen, M. A. T., & Girardi, L. 2009, Astronomy & Astrophysics, 498, 95

Villalobos, Á., & Helmi, A. 2008, Monthly Notices of the Royal Astronomical Society, 391, 1806

Watkins, L. L., Evans, N. W., Belokurov, V., et al. 2009, Monthly Notices of the Royal Astronomical Society, 398, 1757

Yanny, B., Newberg, H. J., Johnson, J. A., et al. 2009, The Astrophysical Journal, 700, 1282

Zoccali, M., Renzini, A., Ortolani, S., et al. 2003, Astronomy & Astrophysics, 399, 931

AFFILIATIONS

[1] *Laboratório Interinstitucional de e-Astronomia - LIneA, Rua Gal. José Cristino 77, Rio de Janeiro, RJ - 20921-400, Brazil*

[2] *Observatório Nacional, Rua Gal. José Cristino 77, Rio de Janeiro, RJ - 20921-400, Brazil*

[3] *Osservatorio Astronomico di Padova, INAF, Vicolo dell'Osservatorio 5, I-35122 Padova, Italy*
[4] *Kapteyn Astronomical Institute, University of Groningen, Landleven 12, 9747 AD Groningen, The Netherlands*
[5] *Instituto de Física, UFRGS, Caixa Postal 15051, Porto Alegre, RS - 91501-970, Brazil*
[6] *Centro de Investigaciones Energéticas, Medioambientales y Tecnológicas (CIEMAT), Madrid, Spain*
[7] *George P. and Cynthia Woods Mitchell Institute for Fundamental Physics and Astronomy, and Department of Physics and Astronomy, Texas A&M University, College Station, TX 77843, USA*
[8] *LSST 933 North Cherry Avenue, Tucson, Arizona 85721, USA*
[9] *Koninklijke Sterrenwacht van België, Ringlaan 3, B1180 Brussels, Belgium*
[10] *Fermi National Accelerator Laboratory, P. O. Box 500, Batavia, IL 60510, USA*
[11] *Kavli Institute for Cosmological Physics, University of Chicago, Chicago, IL 60637, USA*
[12] *Department of Physics, ETH Zurich, Wolfgang-Pauli-Strasse 16, CH-8093 Zurich, Switzerland*
[13] *Instituto de Fisica Teorica UAM/CSIC, Universidad Autonoma de Madrid, 28049 Madrid, Spain*
[14] *CNRS, UMR 7095, Institut d'Astrophysique de Paris, F-75014, Paris, France*
[15] *Sorbonne Universités, UPMC Univ Paris 06, UMR 7095, Institut d'Astrophysique de Paris, F-75014, Paris, France*
[16] *Department of Physics & Astronomy, University College London, Gower Street, London, WC1E 6BT, UK*
[17] *Kavli Institute for Particle Astrophysics & Cosmology, P. O. Box 2450, Stanford University, Stanford, CA 94305, USA*
[18] *SLAC National Accelerator Laboratory, Menlo Park, CA 94025, USA*
[19] *Department of Astronomy, University of Illinois at Urbana-Champaign, 1002 W. Green Street, Urbana, IL 61801, USA*
[20] *National Center for Supercomputing Applications, 1205 West Clark St., Urbana, IL 61801, USA*
[21] *Institut de Física d'Altes Energies (IFAE), The Barcelona Institute of Science and Technology, Campus UAB, 08193 Bellaterra (Barcelona) Spain*
[22] *Department of Physics, IIT Hyderabad, Kandi, Telangana 502285, India*
[23] *Department of Astronomy/Steward Observatory, University of Arizona, 933 North Cherry Avenue, Tucson, AZ 85721-0065, USA*
[24] *Jet Propulsion Laboratory, California Institute of Technology, 4800 Oak Grove Dr., Pasadena, CA 91109, USA*
[25] *Institut d'Estudis Espacials de Catalunya (IEEC), 08034 Barcelona, Spain*
[26] *Institute of Space Sciences (ICE, CSIC), Campus UAB, Carrer de Can Magrans, s/n, 08193 Barcelona, Spain*
[27] *Department of Astronomy, University of Michigan, Ann Arbor, MI 48109, USA*
[28] *Department of Physics, University of Michigan, Ann Arbor, MI 48109, USA*
[29] *Department of Physics, Stanford University, 382 Via Pueblo Mall, Stanford, CA 94305, USA*
[30] *Santa Cruz Institute for Particle Physics, Santa Cruz, CA 95064, USA*
[31] *Center for Cosmology and Astro-Particle Physics, The Ohio State University, Columbus, OH 43210, USA*
[32] *Department of Physics, The Ohio State University, Columbus, OH 43210, USA*
[33] *Harvard-Smithsonian Center for Astrophysics, Cambridge, MA 02138, USA*
[34] *Australian Astronomical Optics, Macquarie University, North Ryde, NSW 2113, Australia*
[35] *Institució Catalana de Recerca i Estudis Avançats, E-08010 Barcelona, Spain*
[36] *Department of Astrophysical Sciences, Princeton University, Peyton Hall, Princeton, NJ 08544, USA*
[37] *Brookhaven National Laboratory, Bldg 510, Upton, NY 11973, USA*
[38] *School of Physics and Astronomy, University of Southampton, Southampton, SO17 1BJ, UK*
[39] *Brandeis University, Physics Department, 415 South Street, Waltham MA 02453*
[40] *Instituto de Física Gleb Wataghin, Universidade Estadual de Campinas, 13083-859, Campinas, SP, Brazil*
[41] *Computer Science and Mathematics Division, Oak Ridge National Laboratory, Oak Ridge, TN 37831*
[42] *Institute of Cosmology and Gravitation, University of Portsmouth, Portsmouth, PO1 3FX, UK*
[43] *Argonne National Laboratory, 9700 South Cass Avenue, Lemont, IL 60439, USA*
[44] *Cerro Tololo Inter-American Observatory, National Optical Astronomy Observatory, Casilla 603, La Serena, Chile*